ACS central science

Research Article

Cite This: ACS Cent. Sci. 2019, 5, 558−568

http://pubs.acs.org/journal/acscii

An Unconventional Iron Nickel Catalyst for the Oxygen Evolution Reaction

Fang Song,[†,‡] Michael M. Busch,[§] Benedikt Lassalle-Kaiser,[∥] Chia-Shuo Hsu,[⊥] Elitsa Petkucheva,[†,#] Michaël Bensimon,[▽] Hao Ming Chen,*[,⊥] Clemence Corminboeuf,*[,§] and Xile Hu*[,†]

[†]Laboratory of Inorganic Synthesis and Catalysis, Institute of Chemical Sciences and Engineering, Ecole Polytechnique Fédérale de Lausanne (EPFL), EPFL−ISIC−LSCI, BCH 3305, Lausanne CH 1015, Switzerland

[‡]State Key Laboratory of Metal Matrix Composites, School of Materials Science and Engineering, Shanghai Jiao Tong University, Shanghai 200240, China

[§]Laboratory for Computational Molecular Design, Institute of Chemical Sciences and Engineering, and National Center for Computational Design and Discovery of Novel Materials (MARVEL), Ecole Polytechnique Fédérale de Lausanne (EPFL), Lausanne CH 1015, Switzerland

[∥]Synchrotron SOLEIL, L'Orme des Merisiers, Saint-Aubin, 91191 Gif-sur-Yvette, France

[⊥]Department of Chemistry, National Taiwan University, Taipei 10617, Taiwan

[#]Department of PEM Hydrogen Systems, Acad. E. Budevski Institute of Electrochemistry and Energy Systems (IEES), Acad. G. Bonchev Str. Bl.10, Sofia 1113, Bulgaria

[▽]General Environmental Laboratory, Institute of Environmental Engineering, Ecole Polytechnique Fédérale de Lausanne (EPFL), Lausanne 1015, Switzerland

Supporting Information

ABSTRACT: The oxygen evolution reaction (OER) is a key process that enables the storage of renewable energies in the form of chemical fuels. Here, we describe a catalyst that exhibits turnover frequencies higher than state-of-the-art catalysts that operate in alkaline solutions, including the benchmark nickel iron oxide. This new catalyst is easily prepared from readily available and industrially relevant nickel foam, and it is stable for many hours. Operando X-ray absorption spectroscopic data reveal that the catalyst is made of nanoclusters of γ-FeOOH covalently linked to a γ-NiOOH support. According to density functional theory (DFT) computations, this structure may allow a reaction path involving iron as the oxygen evolving center and a nearby terrace O site on the γ-NiOOH support oxide as a hydrogen acceptor.

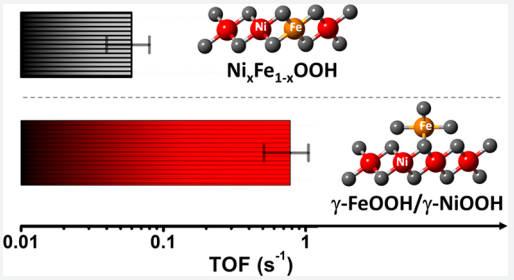

1. INTRODUCTION

The water splitting reaction provides a convenient process through which intermittent renewable energies are stored in the form of chemical fuels, namely, hydrogen and oxygen.[1] Although numerous transition metal oxides have been explored as catalysts for the oxygen evolution reaction (OER, $2H_2O \rightarrow O_2 + 4H^+ + 4e^-$),[2−4] this reaction remains a bottleneck in the water splitting reaction. While only precious IrO_x, RuO_x, and their composites have sustained OER activity in acidic solutions, a number of nonprecious metal oxides are reported to have higher activity than IrO_x[5−12] in alkaline solutions. Among these catalysts, nickel iron oxide ($NiFeO_x$) is widely considered as the benchmark catalyst.[4,9,11−16] This catalyst has a simple binary composition and exhibits turnover frequencies (TOFs) up to about 0.5 s^{-1} at an overpotential of 300 mV, higher than nearly all reported catalysts.[9,11] A recent study showed that $NiFeO_x$ models derived from mass-selected NiFe nanoparticles have a bulk TOF of as high as 1.2 s^{-1} at an overpotential of 300 mV.[16] While the high activity of $NiFeO_x$ is well-established, there is a vivid debate in the nature of the active site, especially whether Fe or Ni is the active metal.[12,14,17−25]

Here, we describe an iron nickel oxide catalyst that exhibits a TOF significantly higher than state-of-the-art $NiFeO_x$ catalysts. This catalyst is stable and can be easily prepared from nickel foam (NF), a readily available and industrially relevant substrate. Through a chemical pretreatment step, we are able to translate the high TOFs into high geometric activity, yielding electrodes that deliver 10 and 100 mA cm^{-2} at overpotentials of only 215 and 248 mV, respectively. Operando X-ray absorption spectroscopy reveals a unique structure of this catalyst consisting of nanoclusters of γ-FeOOH covalently linked to a γ-NiOOH support, which is formed in situ on NF. DFT computations suggest that this structure may open up a

Received: January 18, 2019
Published: February 26, 2019

DOI: 10.1021/acscentsci.9b00053
ACS Cent. Sci. 2019, 5, 558−568

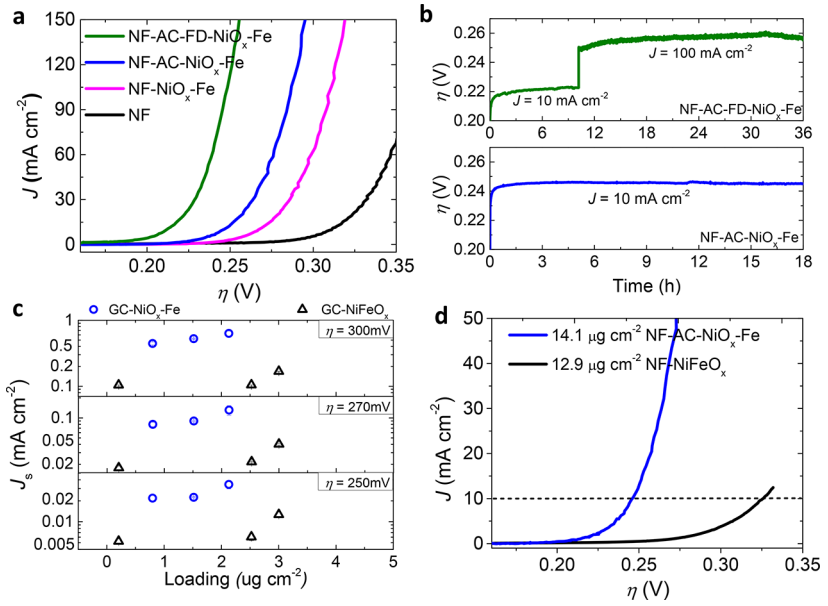

Figure 1. Activity and stability of catalysts. (a) Polarization curves of NF (black), NF-NiO$_x$-Fe (magenta), NF-AC-NiO$_x$-Fe (blue), and NF-AC-FD-NiO$_x$-Fe (green). Loadings of iron oxide in NF-NiO$_x$-Fe, NF-AC-NiO$_x$-Fe, and NF-AC-FD-NiO$_x$-Fe are 4.3, 14.1, and 68.0 μg cm^{-2}, respectively. Backward scan; scan rate, 1 mV s^{-1}; IR-corrected. (b) Chronopotentiometric measurements of the OER at 10 mA cm^{-2} for 18 h using NF-AC-NiO$_x$-Fe (bottom) as catalyst and at 10 and 100 mA cm^{-2} for 36 h using NF-AC-FD-NiO$_x$-Fe (top) as catalyst. (c) The J_s at different loadings of Fe_2O_3 for GC-NiO$_x$-Fe (blue spheres) and GC-NiFeO$_x$ (black triangles). (d) Comparison of polarization curves between NF-AC-NiO$_x$-Fe and NF-NiFeO$_x$ at similar loading.

bifunctional reaction pathway facilitating the O−O bond formation.

2. RESULTS AND DISCUSSION

2.1. Synthesis and Activity of Catalysts. NF is widely used as a 3-dimensional support for OER catalysts,[10,26] but its intrinsic activity is modest (Figure 1a). Since it had been shown that iron incorporation is required to enhance the OER activity of NiO$_x$-based catalysts,[11,14,27,28] we hypothesized that the activity of NF might be increased in a similar way by iron incorporation. Fe ions were incorporated by potential cycling in commercial KOH, as it was previously shown that such a process led to the incorporation of Fe ions into NiO$_x$ films.[11] Indeed when NF was subjected to 100 repetitive cyclic voltammetric (CV) scans from 1.21 to 1.54 V versus the reversible hydrogen electrode (RHE) in a 1 M commercial KOH solution (with an Fe concentration of 0.18 mg L^{-1} according to measurements using inductively coupled plasma mass spectrometry (ICP-MS)), a layer of Fe-containing nickel oxide (NiO$_x$-Fe) was formed. A NF-NiO$_x$-Fe electrode (loading of iron oxide: 4.3 μg cm^{-2}) exhibits much higher OER activity than NF (Figure 1a). The as-received NF was then immersed into a solution containing 10 wt % hydrochloric acid (HCl) for 30 min, which resulted in a NF-AC (AC = acid-cleaned) electrode with a rougher surface than NF according to the scanning electron microscopy images (Figure S1). After repetitive CV or linear sweep voltammetric (LSV) scans from 1.21 to 1.54 V versus RHE in a 1 M commercial KOH solution, NF-AC-NiO$_x$-Fe electrodes were prepared. According to ICP-MS, the iron oxide loadings were in the range 1.0−14.1 μg cm^{-2} depending on the preparation procedure (details are provided in the Experimental Section).

The NF-AC-NiO$_x$-Fe electrodes exhibit excellent OER activity (Figure 1a and Figure S2a). To reach 10 mA cm^{-2}, a NF-AC-NiO$_x$-Fe electrode (loading of iron oxide: 14.1 μg cm^{-2}) requires an overpotential of 245 mV, lower than NF-NiO$_x$-Fe (266 mV) and NF (311 mV). The Tafel slopes are 34, 36, and 45 mV dec^{-1} for NF-AC-NiO$_x$-Fe, NF-NiO$_x$-Fe, and NF, respectively (Figure S3). The activity of the NF-AC-NiO$_x$-Fe electrode is stable: the overpotential for a current density of 10 mA cm^{-2} remained at 245 mV during an electrolysis of 18 h (Figure 1b). When NF-AC was subjected to 100 CV scans in a 1 M KOH solution that was stripped of Fe ions by sequestration with an excess of nickel hydroxides for 12 h (the Fe concentration was below the detection limit of ICP-MS after the treatment), the resulting Fe-free NF-AC-NiO$_x$ exhibited much lower OER activity (Figure S4). Thus, Fe incorporation was essential for the high OER activity of the NF-AC-NiO$_x$-Fe and NF-NiO$_x$-Fe electrodes.

By using commercial KOH solution which contained only a trace amount of Fe ions, the maximum amount of Fe incorporation into NF-AC electrodes was limited to about 14 μg cm^{-2}. Although this method of Fe incorporation seemed to be important for the optimal distribution of Fe active sites and the corresponding site-averaged activity (see below), the geometrically averaged activity might benefit from a higher loading of Fe. Such activity is relevant to practical applications, especially because Fe is cheap. To incorporate more Fe in NF-AC, we dipped the latter into an $FeCl_3$ solution (0.01 M) for 15 min and then dried it in an oven at 70 °C. The resulting electrode, NF-AC-FD (FD = Fe dipping), has hierarchical nanoporous structures at the surface (Figure S5). NF-AC-FD was subjected to 100 repetitive cyclic voltammetric (CV) scans from 1.21 to 1.53 V versus RHE in a 1 M commercial KOH solution to yield the NF-AC-FD-NiO$_x$-Fe electrode. This electrode has much better net activity than NF-AC-NiO$_x$-Fe, reaching 10 and 100 mA cm^{-2} at only 215 and 248 mV (Figure 1a), respectively. The activity is stable for 36 h at least (Figure 1b).

DOI: 10.1021/acscentsci.9b00053
ACS Cent. Sci. 2019, 5, 558−568

Table 1. Comparison of TOFs and J_s of Selected State-of-the-Art OER Catalysts in Alkaline Solutions[a]

		overpotential				
		270 mV		300 mV		
catalysts	electrode	TOF (s^{-1})	J_s (mA cm^{-2})	TOF (s^{-1})	J_s (mA cm^{-2})	ref
NF-AC-NiO_x-Fe	NF	0.78 ± 0.27	0.041 ± 0.018	3.4 ± 1.1	0.18 ± 0.08	this work
NF-AC-FD-NiO_x-Fe	NF	0.82 ± 0.13	0.051 ± 0.008	n/a	n/a	this work
Au-NiO_x-Fe	Au	0.73 ± 0.23	0.17 ± 0.03	3.5 ± 1.3	0.81 ± 0.17	this work
GC-NiO_x-Fe	GC	0.48 ± 0.10	0.10 ± 0.03	2.5 ± 0.44	0.54 ± 0.09	this work
NF-$NiFeO_x$[b]	NF	0.06 ± 0.02	0.012 ± 0.002	0.33 ± 0.06	0.05 ± 0.01	this work
GC-$NiFeO_x$[b]	GC	0.10 ± 0.02	0.03 ± 0.01	0.44 ± 0.05	0.13 ± 0.04	this work
$NiFeO_x$[c]	GC/Au	0.072 ± 0.02[e]	0.011[e]	0.52 ± 0.16	0.084	9 and 11
$NiFeO_x$	Au	n/a	0.015 ± 0.010[e]	n/a	0.11 ± 0.07[e]	8
NiFe LDH	GC	0.036	n/a	0.21	n/a	7
G-FeCoW	GC	n/a	n/a	0.93	n/a	10
IrO_2[d]	Au	~0.002[e]	0.004[e]	~0.01	0.02	6 and 8

[a]For multiple samples, the averaged values with standard deviations are given. For NF-AC-NiO_x-Fe, Au-NiO_x-Fe, and GC-NiO_x-Fe, each sample is measured 2−3 times, and the raw data are shown in Tables S1−S3. For all iron-containing samples except G-FeCoW, iron is assumed as the active species; for G-FeCoW, Co is taken as the active species. n/a indicates not available, due to lack of data or influence by mass transfer. [b]$NiFeO_x$ was prepared according to the method reported in the literature[11] (Experimental Section). Each sample is measured 2 times, and the raw data are shown in Table S4. [c]TOFs were taken from the samples on GC reported in the literature.[11] J_s values are taken from the continuously deposited film on Au reported in the literature[9] (for a calculation of J_s, see the Supporting Information). These numbers represent the highest reported numbers among various samples (see Table S6). [d]TOFs are taken from the literature,[6] and J_s values are taken from the literature.[8] [e]TOFs and J_s at these potentials are extrapolated using the reported Tafel slopes (~35 mV dec^{-1} for $NiFeO_x$, ~40 mV dec^{-1} for IrO_2).

Three figures of merit including turnover frequency (TOF), surface-area-averaged specific activity, and overpotential for 10 mA cm^{-2} are commonly used to compare OER catalysts.[4,8] The first two parameters focus on the intrinsic activity of catalysts, while the third one is oriented toward device performance. These three parameters were determined for the catalyst reported here and compared to the best performing OER catalysts in alkaline solutions (Table 1, Tables S1−S9). It appears that this catalyst outperforms all other catalysts for at least 2 of these parameters and competes well for all of them.

As spectroscopic data (see below) indicate that the active site of our catalyst is a dimeric Ni−Fe unit, the apparent TOFs of the NF-AC-NiO_x-Fe electrodes were calculated according to the total amount of this unit, which was identical to the amount of Fe ions, as determined by ICP-MS (Figure S6 and Table S1, Supporting Information). TOFs were calculated for 10 different electrodes with an Fe (Fe oxide) loading in the range 1.4−14.1 $\mu g\ cm^{-2}$, and were found to be similar. Table 1 compares the averaged TOFs of NF-AC-NiO_x-Fe with several state-of-the-art catalysts, and Tables S5 and S6 list the comparison with an extended number of known catalysts. All TOFs were calculated according to the total amounts of active metal ions. NF-AC-NiO_x-Fe and NF-AC-FD-NiO_x-Fe have similar TOFs. Their TOFs are the highest among all solid-state catalysts reported to date. With an average TOF of 0.78 s^{-1} at η = 270 mV, NF-AC-NiO_x-Fe is multiple times more active than state-of-the-art $NiFeO_x$ and NiFe LDH catalysts[7,11] and about 2 orders of magnitude more active than IrO_2. Recently a gelled FeCoW oxyhydroxide (G-FeCoW) was reported to be the hitherto most active OER catalyst in alkaline solutions.[10] NF-AC-NiO_x-Fe has a TOF substantially higher than G-FeCoW as well. To alleviate the uncertainty using literature values when comparing TOFs, direct comparison of NF-AC-NiO_x-Fe with $NiFeO_x$ deposited on NF was conducted (Tables S4 and S5). The TOFs of NF-AC-NiO_x-Fe are again multiple times higher than those of NF-$NiFeO_x$.

In the above calculation of TOFs for NF-AC-NiO_x-Fe and NF-AC-FD-NiO_x-Fe, the NiO_x component was treated as a support for the active Fe−Ni units. For this assumption to be valid, the TOFs should be independent of the quantity of NiO_x. For verification of this assumption, thin layers of NiO_x were first electrodeposited on Au and glassy carbon (GC) electrodes, followed by iron incorporation using the same method as for the synthesis of NF-AC-NiO_x-Fe. On these two electrodes, the quantity of NiO_x could be varied and measured. The activities of the resulting catalysts, Au-NiO_x-Fe and GC-NiO_x-Fe, were measured by LSV (Figure S7). Notwithstanding a small difference, both Au-NiO_x-Fe and GC-NiO_x-Fe exhibit activities and TOFs (Table 1, Figure S7 and Tables S1−S3) similar to NF-AC-NiO_x-Fe. The small difference is likely due to the electrical contact between the NiO_x film and the electrodes rather than the intrinsic activity of the catalyst. The TOFs of Au-NiO_x-Fe and GC-NiO_x-Fe are largely independent of the quantity of NiO_x (Figure S8). These data validate the treatment of NiO_x as a support in the calculation of TOFs of our catalysts and show that it outperforms all alkaline OER catalysts reported so far.

The specific activity (J_s), which is the current density averaged by the electrochemical surface area, is a parameter that is complementary to TOF in evaluating the intrinsic activity of electrocatalysts.[8] For a direct comparison, the specific activities of our NiO_x-Fe catalyst and $NiFeO_x$ deposited on the same supports (NF and GC) were measured (Supporting Information). It was previously reported that $NiFeO_x$ had the highest specific activity among various transition metal oxides.[8] On both electrodes, our catalyst has substantially higher specific activity than $NiFeO_x$ (Figure 1c, Table 1, and Table S7). The specific activity on GC is higher than on NF for both catalysts because electrochemical surface areas correspond only to those of the catalysts due to the GC's flat surface, while on NF the areas correspond to those of the porous NF electrodes. The values on GC are therefore representative of the true activity of the catalysts. For the $NiFeO_x$ catalyst, our value is similar to those determined in the literature,[8,9] confirming that the $NiFeO_x$ catalyst used in the direct comparison exhibits the same activity as the state-of-the-

DOI: 10.1021/acscentsci.9b00053
ACS Cent. Sci. 2019, 5, 558−568

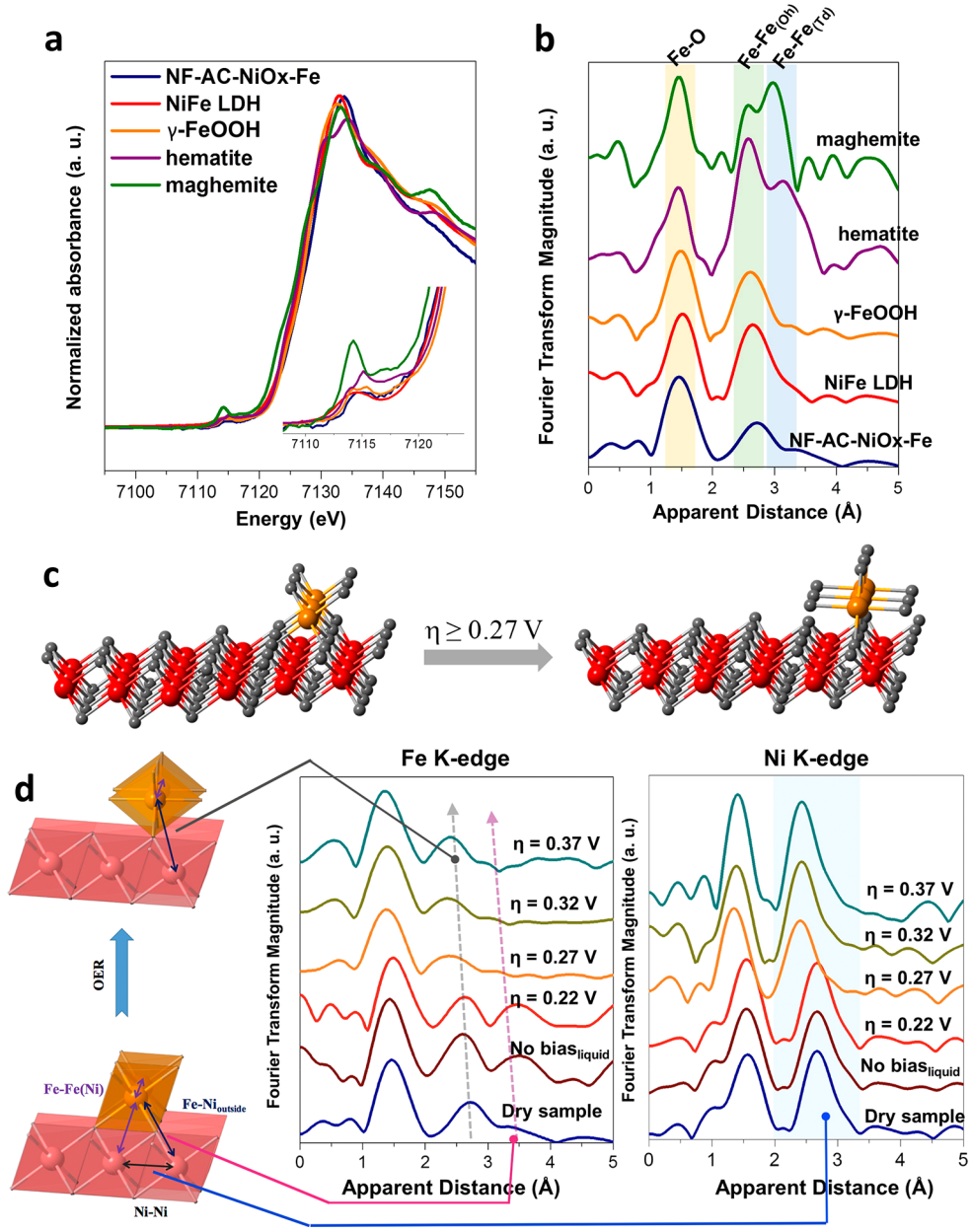

Figure 2. In situ X-ray absorption spectroscopy. (a) XANES spectra, inset shows the pre-edge features of all spectra. (b) Fourier transform of Fe K-edge EXAFS spectra for NF-AC-NiO$_x$-Fe and the corresponding references. (c) Proposed structural model of NF-AC-NiO$_x$-Fe showing γ-FeOOH sitting on the surface of NiOOH; upon application of an overpotential of more than 0.27 V the structure reorganizes with a tilt. (d) In situ FT-EXAFS spectra of Fe K-edge and Ni K-edge for Au-NiO$_x$-Fe during the OER.

art samples. The intrinsic activity of the NiO$_x$-Fe catalysts is therefore superior to all known catalysts for which an intrinsic activity has been reported.

It should be pointed out that comparison of different catalysts by TOF and specific activity is not straightforward. The measured performance is influenced by the experimental procedures and the ensuring data analysis. Thus, while the above analysis is done using standard practices in the field, the 10 times higher TOF and 3−4 times higher specific activity of our catalyst compared to conventional NiFeO$_x$ should not be taken literally. The main conclusion of this comparison is that the present NiO$_x$-Fe catalyst is significantly more active than NiFeO$_x$.

Another important parameter of catalytic activity is the overpotential for a given current density, e.g., 10 mA cm^{-2} (Table S8). In direct comparison and at similar loadings, the present NiO$_x$-Fe catalyst has overpotentials of about 74−80 mV lower than NiFeO$_x$ (Figure 1d, and Figure S9). A striking improvement of more than 160 mV in overpotential is obtained when comparing NF-AC-NiO$_x$-Fe with IrO$_2$, the benchmark noble metal catalyst, at a similar loading. A small number of high-surface-area electrodes coated with a large amount of catalysts are reported to have overpotentials close to 200 mV for 10 mA cm^{-2}, making them interesting for device performance (Table S9).[10,26,29] With an overpotential of only 215 mV, stable activity, and an easy and economical preparation from earth-abundant components, the NF-AC-FD-NiO$_x$-Fe electrode described above is also competitive in this category. It should be noted that our synthetic procedure can be easily adapted for the activation of various Ni-based

DOI: 10.1021/acscentsci.9b00053
ACS Cent. Sci. 2019, 5, 558−568

Table 2. Structural Parameters of Au-NiO$_x$-Fe Sample Extracted from In Situ Fe K-edge EXAFS Refinement during the OER

condition	path	R (Å)	CN	ΔE (eV)	σ^2 (Å^2)	R-value (%)
dry powder	Fe−O	1.98(1)	4.8(2)	0.1(8)	0.0090(2)	7.801
	Fe−Fe(Ni)	3.10(2)	5.0(2)	1.8(6)	0.0115(1)	
	Fe−Ni$_{outside}$	3.98(4)	3.8(4)	1.6(7)	0.0051(6)	
no bias	Fe−O	1.93(1)	5.3(2)	−0.7(1)	0.0100(2)	7.810
	Fe−Fe(Ni)	3.01(2)	5.0(2)	4.8(1)	0.0060(1)	
	Fe−Ni$_{outside}$	3.83(4)	3.5(9)	−0.8(2)	0.0028(6)	
0.22	Fe−O	1.98(3)	5.3(1)	0.3(3)	0.0034(1)	5.906
	Fe−Fe(Ni)	3.04(4)	5.0(1)	−4.1(3)	0.0088(2)	
	Fe−Ni$_{outside}$	3.80(9)	3.5(1)	−2.4(4)	0.0024(3)	
0.27	Fe−O	1.91(1)	4.3(4)	−4.0(1)	0.0103(1)	3.800
	Fe−Fe(Ni)	2.87(3)	2.3(3)	−4.4(1)	0.0120(4)	
	Fe−Ni$_{outside}$	3.34(4)	2.1(7)	−1.6(3)	0.0138(9)	
0.32	Fe−O	1.93(1)	4.9(1)	−1.7(3)	0.0103(2)	1.907
	Fe−Fe(Ni)	2.88(2)	2.3(6)	−2.9(3)	0.0108(4)	
	Fe−Ni$_{outside}$	3.22(6)	2.2(9)	−3.2(5)	0.0123(7)	
0.37	Fe−O	1.91(1)	4.7(4)	−2.9(8)	0.0103(1)	11.580
	Fe−Fe(Ni)	2.86(2)	3.1(2)	2.7(7)	0.0118(1)	
	Fe−Ni$_{outside}$	3.21(5)	1.9(7)	1.0(1)	0.0135(4)	

electrodes, making it industrially relevant as Ni electrodes are used in commercial electrolyzers.

2.2. Characterization of Catalysts Including Operando XAS. The NiO$_x$-Fe catalyst was subjected to a variety of characterization methods. X-ray photoelectron spectroscopy (XPS) data are consistent with the presence of iron oxide on the surface of the electrode (Figure S10).[30] In the Raman spectra, the peaks corresponding to γ-NiOOH, initially absent in the catalyst before the OER, emerged after subjecting the catalyst to OER conditions (Figure S11). This lamellar structure has already been shown to be the active phase in nickel-containing OER catalysts under oxidative potentials.[31] No peak from an iron oxide species was, however, observed in the Raman spectra, probably because of the low iron concentration. To obtain further structural information on the catalyst, X-ray absorption spectroscopy (XAS) was applied, both on the postcatalytic material and under operating conditions.

Figure 2a shows the Fe K-edge X-ray absorption near-edge spectra (XANES) of NF-AC-NiO$_x$-Fe, together with iron oxide and NiFe LDH references.[32] The oxidation state of as-prepared NF-AC-NiO$_x$-Fe is close to the value of +3, since the main absorption edge position coincides with that of γ-Fe(3+)OOH. Spinel iron oxides (maghemite and magnetite) and hematite contain both octahedral and tetrahedral sites. Tetrahedral iron sites have a well-defined signature in the Fe K-pre-edge with an intense peak at low energies (ca. 7114 eV).[33,34] From the pre-edge intensity and position (inset of Figure 2a), the tetrahedrally coordinated Fe ions can therefore be ruled out. This result is confirmed by extended X-ray absorption fine structure (EXAFS) spectra at the Fe K-edge (as depicted in Figure 2b), which further describes the local geometry of Fe. The first peak at apparent distances 1.5 Å, and the second and third peaks at 2.5 and 3.1 Å, are attributed to the single scattering path of the closest oxygen (that is, Fe−O) and the second/third neighboring iron metals (that is, Fe−Fe(Ni)) surrounding the absorbing Fe ions,[35,36] respectively. These results clearly reveal the Fe−Fe bonds with octahedrally coordinated Fe ions in NF-AC-NiO$_x$-Fe, which are more similar to those of γ-FeOOH or NiFe-LDH and Fe-doped γ-NiOOH,[14] as opposed to hematite or spinel structures.

Most interestingly, a new peak (Fe−Ni$_{outside}$) was observed at 3.98 Å (Figure 2b, Table 2, Tables S10 and S11, and Figures S12−S14); this value is significantly larger than those of both Fe−Fe$_{(Td)}$ and Fe−Fe$_{(Oh)}$ in hematite or spinel structures, as well as that of Fe−Ni in NiFe LDH (~3.1 Å), indicating that there is an Fe−Ni path with a specific long distance in NF-AC-NiO$_x$-Fe (~4.0 Å). The coordination number (CN) of Fe−Fe is remarkably smaller than those of Lepidocrocite (γ-FeOOH) or NiFe-LDH. This result reveals small size clusters (~1−2 nm), where the Fe ions at the edges have fewer Fe−Fe(Ni) interactions than in the center (Table S10 and Figures S13 and S14), thus decreasing the overall mean Fe−Fe coordination numbers. With the CNs taken into account, a structural model is proposed as below. First, we consider the dry sample (before the OER). The support has the structure of NiO. In our fitting, the CNs are only 5.0 and 3.8 for Fe−Fe(Ni) path (edge-sharing MO_6 octahedrons: ~3.1 Å) and Fe−Ni$_{outside}$ path (corner-sharing MO_6 octahedrons: ~4.0 Å), respectively. These CN numbers indicate that Fe ions are not located in the bulk of NiO because otherwise the CNs for Fe−Fe(Ni) path and Fe−Ni$_{outside}$ path will be 12 and 6, respectively. Instead, there are three possible locations for the Fe ions: (i) on the surface (Figure S15a); (ii) on step I (Figure S15b); and (iii) on step II (Figure S15c) of the (111) facet of NiO. The CNs for Fe−Fe(Ni) path and Fe−Ni$_{outside}$ path for these models are shown in Table S12. Assuming that Fe occupies all these three sites before the OER, the CNs of Fe−Fe(Ni) path and Fe−Ni$_{outside}$ path will be in the range 4−8 and 3−5, respectively, which are consistent with our fitting data. The EXAFS spectrum of NF-AC-NiO$_x$-Fe catalyst is different from those of Fe (oxy)hydroxide (FeOOH) and NiFe LDH reference samples, which lack corner-sharing FeO_6. The NF-AC-NiO$_x$-Fe catalyst in the dry form can be described as discrete nanoclusters of γ-FeOOH covalently linked to the NiO$_x$ support via bridging oxygens (Figure 2c).

In situ X-ray absorption spectroscopy was employed to reveal the structural evolution of the catalyst during the OER (Figure 2d, Table 2, and Table S11).[37,38] For the collection of Ni K-edge data, the catalysts deposited on Au-coated fluorine-doped tin oxide (FTO) (Au-NiO$_x$-Fe) were used instead of NF-AC-NiO$_x$-Fe because of the strong background Ni signal

DOI: 10.1021/acscentsci.9b00053
ACS Cent. Sci. 2019, 5, 558−568

from NF. The Fe K-edge data of Au-NiO_x-Fe are similar to those of NF-AC-NiO_x-Fe, confirming the similar nature of catalysts on both supports. Prior to the OER (when no bias or η = 0.22 V is applied), slight decreases in apparent distance are observed compared to the dry sample. These changes might be attributed to a specific interaction with the electrolyte. Once the applied voltage is further increased above η = 0.27 V, the apparent distance of the Fe−Fe(Ni) path is reduced by approximately 0.17 Å. This decrease in Fe−Fe(Ni) path is due to the Fe−O bond contract imposed by the oxidation of NiO substrate (see below), as observed before in other systems.[14,36] Likewise, in situ Ni K-edge XAS (Figure 2d, Figure S16, and Table S11) shows that the apparent distances of the Ni−Ni path are reduced by about 0.24−0.27 Å under OER potentials, indicating the oxidation of Ni ions. The potential-dependent edge energies (Figure S17) indicate the transformation of the NiO_x support to γ-NiOOH under OER conditions,[14,31] in agreement with the result of the Raman study (see above). The different degree of shrinkage between the Fe−Fe(Ni) and Ni−Ni paths as well as between Fe−O (3%) and Ni−O (8%) bonds is consistent with the FeO_6 octahedrons located at the surface sites of NiOOH instead of being fully incorporated as is the case in NiFe LDH and $NiFeO_x$ catalysts. A previous in situ XAS study showed that in $NiFeO_x$ the Fe−Fe(Ni) and Ni−Ni paths shrank to a similar degree, as were the Fe−O and Ni−O bonds under the OER.[14,36]

The distance of the Fe−$Ni_{outside}$ path changes dramatically, from 3.98 Å in the dry sample to 3.80 Å at no bias and η = 0.22 V to 3.34 Å at η = 0.27 V and further to 3.21 Å at η = 0.37 V. Under the OER condition, NiO is transformed into γ-NiOOH, where the (111) facet of NiO is converted to the (001) facet of γ-NiOOH because of similar atomic arrangement. The γ-FeOOH clusters remain the same (Figure S18). CNs of Fe−Fe(Ni) path and Fe−$Ni_{outside}$ path are expected to be about 4−5 and 3, respectively. However, much smaller CNs (ca. 2) were observed under OER condition. A possible explanation is that under OER conditions Fe−O−Ni may break in some regions because of the contraction of Ni−O and anisotropic tension. Previously we observed breaking of single-layered NiFe LDH nanosheets under the OER.[7] The partial breakage gives the FeO_6 octahedrons more structural flexibility so that they can tilt. From the dry sample to the catalyst at the beginning of the OER (η = 0.27 V), the structural change can be accounted for by considering a 52° tilt of the FeO_6 octahedron relative to the NiO_6 octahedron (Figure 2c and Figure S19). A further 3.6° tilt of the FeO_6 octahedron can account for the structural change from η = 0.27 V to η = 0.37 V. While the more than 50° tilt is significant, it seems feasible since the FeO_6 octahedrons in pure γ-FeOOH are tilted at about 23° one over the other (Figure S20). Importantly, this significant structural change only occurs on NF-AC-NiO_x-Fe catalyst, and it is reversible upon removal of potential. The NiFe LDH reference sample, which is considered as the active form of $NiFeO_x$, exhibits no such structural changes according to operando XAS (Figure S21). This comparison further underscores the unique nature of the present NF-AC-NiO_x-Fe catalyst relative to $NiFeO_x$ and the peculiar role of the interaction between the NiOOH support and the discrete FeOOH clusters.

2.3. DFT Computation and Mechanistic Hypothesis. On metal oxides and in alkaline medium, the OER proceeds via multiple surface-bound intermediates including M—OH, M—OOH, and M═O (M denotes a metallic active site). Both single- and dual-site mechanisms have been proposed, depending on the O—O bond-forming step.[2,39] In a representative single-site mechanism (Figure 3a), one metal

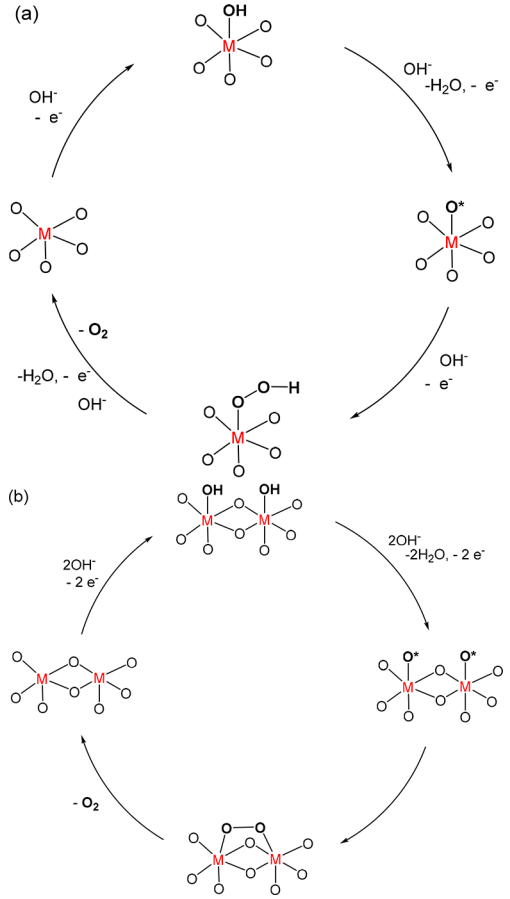

Figure 3. Simplified OER mechanisms. (a) Single-site mechanism. (b) Dual-site mechanism.

site mediates four consecutive hydroxide(proton)-coupled electron transfer steps according to eqs 1−4.[2,5,27,40,41] The O—O bond-forming step is the nucleophilic attack of OH^- on an M═O unit (eq 3). In a representative dual-site mechanism (Figure 3b), two metal sites are involved to support a reaction sequence of eqs 1, 2, 5, and 6.[42−44] The O—O bond-forming step is combination of two M═O units (eq 5). Theoretical and experimental supports for both mechanisms have been reported.[14,21,27,40,42−45] Adding to the complexity is that each electron transfer step in eqs 1−4 is not necessary accompanied by one hydroxide (proton) transfer.[42,46] In other words, each step in Figure 3 might be a sum of two consecutive, uncoupled hydroxide(proton) and electron transfer steps.

$$OH^- + M \rightarrow M{-}OH + e^- \quad (1)$$

$$M{-}OH + OH^- \rightarrow M{=}O + H_2O + e^- \quad (2)$$

$$M{=}O + OH^- \rightarrow M{-}OOH + e^- \quad (3)$$

$$M{-}OOH + OH^- \rightarrow O_2 + H_2O + M + e^- \quad (4)$$

$$M{=}O + M{=}O \rightarrow M{-}O{-}O{-}M \quad (5)$$

$$M{-}O{-}O{-}M \rightarrow 2M + O_2 \quad (6)$$

Many studies have been conducted to probe the active site of $NiFeO_x$;[14,18,20−25] however, there is yet no consensus on

DOI: 10.1021/acscentsci.9b00053
ACS Cent. Sci. 2019, 5, 558−568

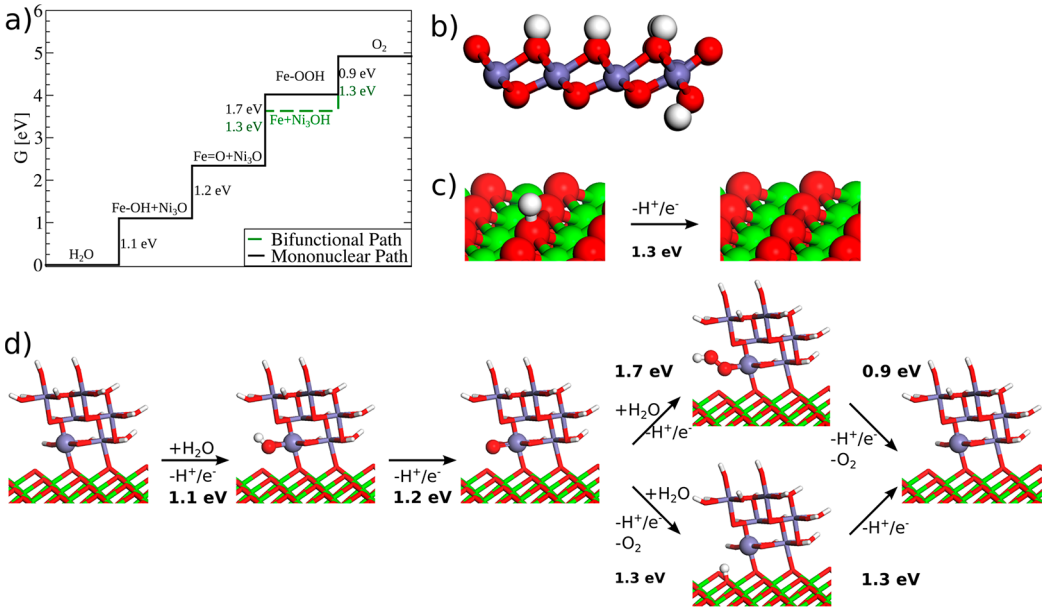

Figure 4. DFT computations. (a) Free energy diagram comparing the electrochemical potentials of water oxidation at γ-FeOOH proceeding through a mononuclear mechanism (black solid line) and a bifunctional mechanism with Ni_3−O sites acting as hydrogen acceptor (green dashed line). (b) Schematic picture of the γ-FeOOH model. Color code: violet, Fe; red, O; gray, H. (c) Ni_3−O hydrogen acceptor site at γ-NiOOH. Color code: green, Ni; red, O; gray, H. (d) Schematic representation of the OER reaction mechanism. Upper path, mononuclear mechanism; lower path, bifunctional mechanism. Color code: violet, Fe; green, Ni; red, O; gray, H.

whether Ni or Fe is the active site. In one proposal, Ni acts as the oxygen evolving site through either high-valent Ni═O or active Ni—O—O^- species,[23−25] while Fe serves as a strong Lewis acid to promote the oxidation at neighboring Ni sites.[25] The O—O bond-forming step is the combination of two Ni═O species.[42] In another proposal, Fe is the active site while Ni provides a conductive matrix.[14,18,20−22,27] The O—O bond-forming step is the nucleophilic attack of OH^- on an Fe═O species.

The present NiO_x-Fe catalyst may operate in a similar mechanism to $NiFeO_x$. The Ni site in γ-NiOOH might be the active site, and the γ-FeOOH clusters lower the potential to generate the reactive Ni═O species via eq 2. According to a previous DFT computations, this step has a theoretical potential of 1.84 V on pure γ-NiOOH.[27] Thus, the γ-FeOOH clusters need to be able to execute a tremendous amount of redox tuning if this mechanism is to operate. Notwithstanding this possibility, we also consider other reaction pathways involving Fe as an active site. We used DFT computations to guide our mechanistic hypothesis (Figure 4). A generic isolated γ-FeOOH cluster was first constructed. This model contains the key features of the active catalyst, i.e., the brucite-type structure and the octahedral coordination by six oxygen ligands (Figure 4b). Computationally, this model has the advantage of representing potentially active Fe sites while avoiding complications resulting from interfacing the cluster with the γ-NiOOH support. On this cluster, the formation of Fe—OH and Fe═O intermediates (eqs 1 and 2) have potentials of 1.1 and 1.2 V, respectively, which are readily accessible under OER conditions. From Fe═O, O_2 might be formed either by combination of two Fe═O units (eqs 5 and 6), or by hydroxide attack of the Fe═O species (eq 3). The first possibility is unlikely because otherwise γ-FeOOH would be an excellent OER catalyst, which is not the case. Considering the second possibility, the potential determining step is then the hydroxide attack on Fe═O, which has a potential of 1.7 V and results in a theoretical overpotential of about 0.5 V (Figure 4a). Thus, γ-FeOOH alone is only a modest catalyst following this pathway, in agreement with experiments.

If the O−O bond-forming step on γ-FeOOH can proceed through an alternative pathway, such as a bifunctional mechanism that avoids the potential limiting formation of Fe-OOH, the overpotential might be reduced.[47] The bifunctional mechanism assumes the direct formation of O_2 through a nucleophilic attack of OH^- coupled with a concerted H transfer to an adjacent acceptor site, A[47−49] (see the section of computational details for the technical treatment of this step):

$$M{=}O + OH^- + A \rightarrow M + O_2 + A{-}H + e^- \quad (7)$$

While rarely proposed in electrocatalysis, this pathway has been observed as a single step in many molecular and enzymatic systems, and is termed as "multisite concerted proton electron transfer".[50,51]

As the Fe ions in NiO_x-Fe are located on the top of the γ-NiOOH support, we explored the H transfer to various nearby sites on γ-NiOOH as potential hydrogen acceptors. It was found that a Ni_3O site at a terrace plane of γ-NiOOH was a suitable hydrogen acceptor, with a potential of 1.3 V for $Ni_3O + H^+ + e^-$ to Ni_3OH (Figure 4c). Such a site is abundantly present at the proximity of the Fe center (Figure 4d). Incorporation of the Ni_3O hydrogen acceptor completely alters the energy landscape of the OER on γ-FeOOH (Figure 4a,d). The O—O bond-forming step now only has a potential of about 1.3 V, resulting in a theoretical overpotential of only 0.1 V. Notwithstanding other possibilities as mentioned above, the bifunctional pathway provides a sensible mechanism that explains the high activity of the present NiO_x-Fe catalyst. Further dedicated studies are required to test this and other mechanisms. Interestingly, a very recent computational study suggested that on the $(\bar{1}2\bar{1}1)$ surface of $NiFeO_x$ the lowest-energy pathway for the O—O bond-forming step involved the

DOI: 10.1021/acscentsci.9b00053
ACS Cent. Sci. 2019, 5, 558−568

attack of a OH^- group of a Ni(III) site to an Fe(IV)═O center with a concomitant hydrogen atom transfer to a neighboring Ni(III) site, very much analogous to eq 7 proposed here.[52]

Although the bifunctional mechanism remains hypothetical for the present catalyst, it provides a new spin in theoretical studies of OER mechanisms. Previous DFT computations suggest that, for catalysts operating by a single-site mechanism, the adsorption energies of OH, O, and OOH are correlated.[40,53] In particular, the difference in the surface adsorption energy of OH and OOH is independent of the catalyst and approximately 3.2 eV.[40,53] This scaling relationship leads to a Volcano plot of catalytic activity with the difference of the absorption energies of O and OH as a descriptor (Figure 5, black line). The minimal theoretical overpotential (η) for

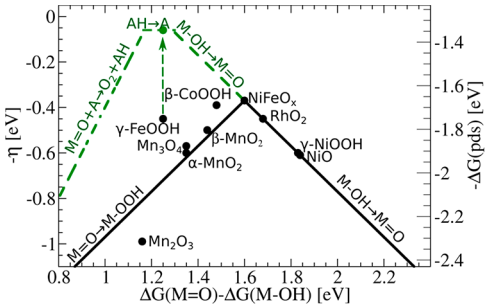

Figure 5. Volcano plots assuming mononuclear (black) and bifunctional OER mechanisms (green). A denotes an arbitrary H acceptor site. γ-FeOOH has been computed in this work while all other oxides were taken from the literature: Mn_3O_4, NiO, RhO_2;[40] β-CoOOH;[45] Mn_2O_3, α-MnO_2, β-MnO_2;[54] $NiFeO_x$, γ-NiOOH.[27]

this type of catalyst is about 0.4 V. According to computations,[10,27,40] on catalysts like NiO, γ-NiOOH, and RhO_2, O binds too weakly which causes the formation of M═O to become potential determining, and the overpotential increases beyond 0.4 V. For catalysts like Mn_3O_4, α-MnO_2, β-MnO_2, IrO_2, and β-CoOOH, O is too strongly bound, and the formation of M═O occurs below 1.6 V.[40,45,54] The potential determining step is the O—O bond formation, which requires more than 1.6 V. The theoretical overpotential is again larger than 0.4 V. For $NiFeO_x$, both steps 2 and 3 occur at about 1.6 V, putting it near the top of a Sabatier-type Volcano plot (Figure 5).[14,27]

The above scaling relationship and the overpotential limit it imposes only hold for catalysts operating by a single-site mechanism. Change of mechanism will overcome this limit. For example, catalysts operating via the dual-site mechanism (Figure 3b), as proposed for certain metal oxides,[39,42] are not constrained by the scaling relationship. The bifunctional mechanism offers another possibility, which is illustrated here using γ-FeOOH as a prototypical example. A concerted H transfer as in eq 7 avoids the formation of the high-energy FeOOH, leading to a new Volcano plot (green curves in Figure 5; see also Figure S22). The left slope represents a region where the O−O bond formation through eq 7 determines the overpotential. A narrow plateau is found at the top of this Volcano plot, where the overpotential is determined by the recovery of the H acceptor site.

3. CONCLUSION

In summary, an iron nickel catalyst with excellent activity for the OER in alkaline solutions has been discovered. This catalyst outperforms the current state-of-the-art $NiFeO_x$ catalyst. It is easily prepared and exhibits long-term stability. Applications can be envisioned for both alkaline electrolyzers and photoelectrochemical water splitting devices, which often employ thin layers of nickel oxide as catalysts, heterojunction, or protection layers.[55−59] Spectroscopic characterization reveals a unique structure of the catalyst comprising nanoclusters of γ-FeOOH covalently linked to a γ-NiOOH support. DFT computations suggest that this structure may allow a bifunctional reaction pathway involving iron as the oxygen evolving center and a nearby terrace O site on the γ-NiOOH support oxide as a hydrogen acceptor.

4. EXPERIMENTAL SECTION

4.1. Reagents and Materials. All reagents were analytical grade and used as received without further purification. Ni foam (with thickness 1.6 mm and 95% porosity) was purchased from Goodfellow Cambridge Ltd. Hydrochloric acid (HCl) and potassium hydroxide (KOH) were purchased from Merck KGaA. The water used throughout all experiments was deionized water.

4.2. Preparation of the Electrodes. For NF, the as-received nickel foam was washed with acetone under sonication condition for 15 min.

For NF-AC, the NF sample was cleaned in 10 wt % HCl under sonication condition for 30 min.

For NF-AC-FD, the NF-AC sample was dipped in 50 mL of freshly prepared $FeCl_3$ solution (0.01 M) under magnetic stirring for 15 min. The NF-AC sample was taken out and directly dried in oven at 70 °C.

For Au-NiO_x, NiO_x was electrodeposited on Au-coated (100 nm) fluorine-doped tin oxide (FTO) substrates (there is a sputtered 10 nm Cr adhesion layer between the Au and FTO layers). The surface area is 1 cm^2. Prior to each deposition, the Au-coated FTO was electrochemically cycled three times from −0.2 to 0.6 V versus Ag/AgCl reference electrode at 10 mV s^{-1} in 1 M Fe free KOH. NiO_x was electrochemically deposited from a nitrogen-purged nickel nitrate solution (0.01 M) at a cathodic current density of 1 mA cm^{-2}, following a modified literature procedure.[60] The typical deposition time was 75 s. For changes in the quantity of NiO_x, the deposition time varied from 75 to 300 s.

For GC-NiO_x, NiO_x was electrodeposited on glassy carbon (GC, the geometric surface area is confined to 0.5 cm^2). The deposition procedure is the same as for Au-coated FTO.

4.3. Preparation of Reference Samples for Raman Test. For γ-FeOOH, 20 mL of $Fe(NO_3)_3$ solution (20 mM) was sealed in a glass container, which was then maintained at 60 °C for 24 h. After centrifuging and washing with water for 3 times, red brown powder of FeOOH was obtained.

γ-NiOOH was synthesized by oxidizing nickel foam with $K_2S_2O_8$ in concentrated NaOH (see ref 61). γ-Fe_2O_3 was obtained by annealing Fe_3O_4 nanoparticles (Sigma-Aldrich, CAS number: 1317-61-9) at 300 °C in air for 12 h. α-Fe_2O_3 was purchased from Fluka (CAS number: 1309-37-1). NiFe LDH was synthesized via a hydrothermal method previously reported by our group (see ref 15).

4.4. Preparation of $NiFeO_x$ Catalysts. To compare with the state-of-the-art $NiFeO_x$ catalyst, we prepared samples of

DOI: 10.1021/acscentsci.9b00053
ACS Cent. Sci. 2019, 5, 558−568

$NiFeO_x$ on GC and NF electrodes following the reported electrodeposition method.[11,13] To avoid the formation of our catalyst during the electrodeposition, the NF was first annealed at 500 °C in air for 2 h. Films of $NiFeO_x$ were cathodically deposited from unstirred solutions of 0.092 M $Ni(NO_3)_2 \cdot 6H_2O$ and 0.008 M $FeCl_2 \cdot 4H_2O$ (or 0.0975 M $Ni(NO_3)_2 \cdot 6H_2O$ and 0.0025 M $FeCl_2 \cdot 4H_2O$) in 18.2 MΩ cm H_2O. The solutions were purged with nitrogen gas for half an hour before adding $FeCl_2 \cdot 4H_2O$ to prevent precipitation of insoluble FeOOH. Typical depositions were at −0.1 mA cm^{-2} for 20−180 s.

4.5. Electrochemical Measurements. Electrochemical characterizations including cyclic voltammetry (CV), linear sweep voltammetry (LSV), and chronopotentiometry were carried out on a Gamry Reference 3000 electrochemical instrument using a three-electrode electrochemical system. A 1 M KOH solution (60 mL) was used as electrolyte, and a Ag/AgCl electrode with saturated KCl filling solution and Pt wire were used as reference and counter electrodes, respectively. Nickel foams were used as working electrodes directly. Hot glue was used to define the working area as a 1.0−1.1 cm^{-2} zone. Before electrochemical measurements, the reference electrode was measured against another unused Ag/AgCl reference electrode stored in saturated KCl solution. Calibration of Ag/AgCl reference electrodes was done by measuring the RHE potential using a Pt electrode under a H_2 atmosphere. During the measurements, Ag/AgCl reference electrode was set into a double-junction electrode to minimize contact between KOH and KCl. CVs were performed at a scan rate of 1 mV s^{-1}, and the average of the two potentials at which the current crossed zero was taken to be the thermodynamic potential for the hydrogen electrode reaction. In 1 M KOH electrolytes, E versus RHE = E versus Ag/AgCl + 1.009 V, and overpotential for OER was η = E versus RHE − 1.23 V = E versus Ag/AgCl − 0.221 V. Ohmic drop correction was performed using the current interrupt (CI) method available in the potentiostat software.

Before the catalytic activity was recorded, catalysts were activated by 5 linear sweeping voltammetry (LSV) scans followed by another 100 cyclic voltammetry scans until reaching a stable state in 1 M KOH (∼30 mL). This process produced ample O_2. Thus, the following voltammetry measurements were conducted in O_2 presaturated solutions. Figure S23 shows a comparison of LSV curves conducted in O_2-saturated and O_2-free solutions. Figure S24 shows LSV curves in O_2-presaturated solutions with and without iR compensation. The LSV scans were recorded in the potential range 0.6−0.38 V versus Ag/AgCl at a scan rate of 1 mV s^{-1}. The cyclic voltammetry scans were recorded in the potential range 0.2−0.53 V versus Ag/AgCl at a scan rate of 10 mV s^{-1}. Following this, 2−3 cycles of backward LSVs were measured at a scan rate of 1 mV s^{-1} to record the catalytic activity. Tafel slopes were calculated on the basis of the LSV curves by plotting overpotential against log(current density). Chronopotentiometric measurements were performed to evaluate the long-term stability. For the loading dependence analysis, loadings were tuned by changing the cycling number of CVs or only applying 1−5 LSVs. In addition to NF-AC, Au-NiO_x and GC-NiO_x were activated using the same procedure.

■ ASSOCIATED CONTENT

Supporting Information

The Supporting Information is available free of charge on the ACS Publications website at DOI: 10.1021/acscentsci.9b00053.

Supplementary methods and computational details including additional details of the characterization, analysis of electrochemical data, XAS data collection and analysis, and DFT structures and computations (PDF)

■ AUTHOR INFORMATION

Corresponding Authors

*E-mail: haomingchen@ntu.edu.tw.
*E-mail: clemence.corminboeuf@epfl.ch.
*E-mail: xile.hu@epfl.ch.

ORCID

Fang Song: 0000-0002-2953-0537
Benedikt Lassalle-Kaiser: 0000-0003-2141-2496
Chia-Shuo Hsu: 0000-0002-7767-8413
Hao Ming Chen: 0000-0002-7480-9940
Clemence Corminboeuf: 0000-0001-7993-2879
Xile Hu: 0000-0001-8335-1196

Notes

The authors declare the following competing financial interest(s): A European priority patent application (16189000.9) titled Method of synthesis of an electrode for use as a catalyst of oxygen evolution reaction was filed by the EPFL with X.L.H., F.S., and E.P. as inventors.
Safety statement: no unexpected or unusually high safety hazards were encountered.

■ ACKNOWLEDGMENTS

This work is supported by the EPFL, the European Research Council (681292), the Zeno Karl Schindler Foundation, and The National Center of Competence in Research (NCCR) "Materials' Revolution: Computational Design and Discovery of Novel Materials (MARVEL)" of the Swiss National Science Foundation (SNSF). We also acknowledge support from the Ministry of Science and Technology, Taiwan (Contracts MOST 107-2628-M-002-015-RSP). Dr. Solenn Reguer, beamline scientist on the DIFFABS beamline at the SOLEIL Synchrotron, is acknowledged for providing XAS spectra of reference samples. We thank Lucas-Alexandre Stern (EPFL) for discussion in synthesis, the Interdisciplinary Center for Electron Microscopy at EPFL for assistance in electron microscopic measurements, and the Material Characterization Platform at EPFL for assistance in Raman spectroscopic measurements.

■ REFERENCES

(1) Lewis, N. S.; Nocera, D. G. Powering the planet: Chemical challenges in solar energy utilization. *Proc. Natl. Acad. Sci. U. S. A.* **2006**, *103*, 15729−15735.
(2) Dau, H.; Limberg, C.; Reier, T.; Risch, M.; Roggan, S.; Strasser, P. The mechanism of water oxidation: From electrolysis via homogeneous to biological catalysis. *ChemCatChem* **2010**, *2*, 724−761.
(3) Han, L.; Dong, S.; Wang, E. Transition-metal (Co, Ni, and Fe)-based electrocatalysts for the water oxidation reaction. *Adv. Mater.* **2016**, *28*, 9266−9291.

DOI: 10.1021/acscentsci.9b00053
ACS Cent. Sci. 2019, 5, 558−568

(4) Song, F.; Bai, L. C.; Moysiadou, A.; Lee, S.; Hu, C.; Liardet, L.; Hu, X. L. Transition metal oxides as electrocatalysts for the oxygen evolution reaction in alkaline solutions: An application-inspired renaissance. *J. Am. Chem. Soc.* **2018**, *140*, 7748−7759.
(5) Suntivich, J.; May, K. J.; Gasteiger, H. A.; Goodenough, J. B.; Shao-Horn, Y. A perovskite oxide optimized for oxygen evolution catalysis from molecular orbital principles. *Science* **2011**, *334*, 1383−1385.
(6) Trotochaud, L.; Ranney, J. K.; Williams, K. N.; Boettcher, S. W. Solution-cast metal oxide thin film electrocatalysts for oxygen evolution. *J. Am. Chem. Soc.* **2012**, *134*, 17253−17261.
(7) Song, F.; Hu, X. Exfoliation of layered double hydroxides for enhanced oxygen evolution catalysis. *Nat. Commun.* **2014**, *5*, 4477.
(8) McCrory, C. C. L.; Jung, S. H.; Peters, J. C.; Jaramillo, T. F. Benchmarking heterogeneous electrocatalysts for the oxygen evolution reaction. *J. Am. Chem. Soc.* **2013**, *135*, 16977−16987.
(9) Batchellor, A. S.; Boettcher, S. W. Pulse-electrodeposited Ni-Fe (oxy)hydroxide oxygen evolution electrocatalysts with high geometric and intrinsic activities at large mass loadings. *ACS Catal.* **2015**, *5*, 6680−6689.
(10) Zhang, B.; Zheng, X. L.; Voznyy, O.; Comin, R.; Bajdich, M.; Garcia-Melchor, M.; Han, L. L.; Xu, J. X.; Liu, M.; Zheng, L. R.; de Arquer, F. P. G.; Dinh, C. T.; Fan, F. J.; Yuan, M. J.; Yassitepe, E.; Chen, N.; Regier, T.; Liu, P. F.; Li, Y. H.; De Luna, P.; Janmohamed, A.; Xin, H. L. L.; Yang, H. G.; Vojvodic, A.; Sargent, E. H. Homogeneously dispersed multimetal oxygen-evolving catalysts. *Science* **2016**, *352*, 333−337.
(11) Trotochaud, L.; Young, S. L.; Ranney, J. K.; Boettcher, S. W. Nickel-iron oxyhydroxide oxygen-evolution electrocatalysts: The role of intentional and incidental iron incorporation. *J. Am. Chem. Soc.* **2014**, *136*, 6744−6753.
(12) Morales-Guio, C. G.; Liardet, L.; Hu, X. Oxidatively electrodeposited thin-film transition metal (oxy)hydroxides as oxygen evolution catalysts. *J. Am. Chem. Soc.* **2016**, *138*, 8946−8957.
(13) Burke, M. S.; Zou, S. H.; Enman, L. J.; Kellon, J. E.; Gabor, C. A.; Pledger, E.; Boettcher, S. W. Revised oxygen evolution reaction activity trends for first-row transition-metal (oxy)hydroxides in alkaline media. *J. Phys. Chem. Lett.* **2015**, *6*, 3737−3742.
(14) Friebel, D.; Louie, M. W.; Bajdich, M.; Sanwald, K. E.; Cai, Y.; Wise, A. M.; Cheng, M. J.; Sokaras, D.; Weng, T. C.; Alonso-Mori, R.; Davis, R. C.; Bargar, J. R.; Norskov, J. K.; Nilsson, A.; Bell, A. T. Identification of highly active Fe sites in (Ni,Fe)OOH for electrocatalytic water splitting. *J. Am. Chem. Soc.* **2015**, *137*, 1305−1313.
(15) Xu, X.; Song, F.; Hu, X. A nickel iron diselenide-derived efficient oxygen-evolution catalyst. *Nat. Commun.* **2016**, *7*, 12324.
(16) Roy, C.; Sebok, B.; Scott, S. B.; Fiordaliso, E. M.; Sørensen, J. E.; Bodin, A.; Trimarco, D. B.; Damsgaard, C. D.; Vesborg, P. C. K.; Hansen, O.; Stephens, I. E. L.; Kibsgaard, J.; Chorkendorff, I. Impact of nanoparticle size and lattice oxygen on water oxidation on $NiFeO_xH_y$. *Nat. Catal.* **2018**, *1*, 820−829.
(17) Burke, M. S.; Enman, L. J.; Batchellor, A. S.; Zou, S.; Boettcher, S. W. Oxygen evolution reaction electrocatalysis on transition metal oxides and (oxy)hydroxides: Activity trends and design principles. *Chem. Mater.* **2015**, *27*, 7549−7558.
(18) Ahn, H. S.; Bard, A. J. Surface interrogation scanning electrochemical microscopy of $Ni_{1-x}Fe_xOOH$ ($0 < x < 0.27$) oxygen evolving catalyst: Kinetics of the "fast" iron sites. *J. Am. Chem. Soc.* **2016**, *138*, 313−318.
(19) Chen, J. Y. C.; Dang, L.; Liang, H.; Bi, W.; Gerken, J. B.; Jin, S.; Alp, E. E.; Stahl, S. S. Operando analysis of NiFe and Fe oxyhydroxide electrocatalysts for water oxidation: Detection of Fe^{4+} by Mössbauer spectroscopy. *J. Am. Chem. Soc.* **2015**, *137*, 15090−15093.
(20) Stevens, M. B.; Trang, C. D. M.; Enman, L. J.; Deng, J.; Boettcher, S. W. Reactive Fe-sites in Ni/Fe (oxy)hydroxide are responsible for exceptional oxygen electrocatalysis activity. *J. Am. Chem. Soc.* **2017**, *139*, 11361−11364.
(21) Goldsmith, Z. K.; Harshan, A. K.; Gerken, J. B.; Vörös, M.; Galli, G.; Stahl, S. S.; Hammes-Schiffer, S. Characterization of NiFe oxyhydroxide electrocatalysts by integrated electronic structure calculations and spectroelectrochemistry. *Proc. Natl. Acad. Sci. U. S. A.* **2017**, *114*, 3050−3055.
(22) Hunter, B. M.; Thompson, N. B.; Müller, A. M.; Rossman, G. R.; Hill, M. G.; Winkler, J. R.; Gray, H. B. Trapping an iron(VI) water-splitting intermediate in nonaqueous media. *Joule* **2018**, *2*, 747−763.
(23) Trześniewski, B. J.; Diaz-Morales, O.; Vermaas, D. A.; Longo, A.; Bras, W.; Koper, M. T. M.; Smith, W. A. In situ observation of active oxygen species in Fe-containing Ni-based oxygen evolution catalysts: The effect of pH on electrochemical activity. *J. Am. Chem. Soc.* **2015**, *137*, 15112−15121.
(24) Görlin, M.; Chernev, P.; Ferreira de Araújo, J.; Reier, T.; Dresp, S.; Paul, B.; Krähnert, R.; Dau, H.; Strasser, P. Oxygen evolution reaction dynamics, Faradaic charge efficiency, and the active metal redox states of Ni−Fe oxide water splitting electrocatalysts. *J. Am. Chem. Soc.* **2016**, *138*, 5603−5614.
(25) Li, N.; Bediako, D. K.; Hadt, R. G.; Hayes, D.; Kempa, T. J.; von Cube, F.; Bell, D. C.; Chen, L. X.; Nocera, D. G. Influence of iron doping on tetravalent nickel content in catalytic oxygen evolving films. *Proc. Natl. Acad. Sci. U. S. A.* **2017**, *114*, 1486−1491.
(26) Luo, J. S.; Im, J. H.; Mayer, M. T.; Schreier, M.; Nazeeruddin, M. K.; Park, N. G.; Tilley, S. D.; Fan, H. J.; Gratzel, M. Water photolysis at 12.3% efficiency via perovskite photovoltaics and earth-abundant catalysts. *Science* **2014**, *345*, 1593−1596.
(27) Diaz-Morales, O.; Ledezma-Yanez, I.; Koper, M. T. M.; Calle-Vallejo, F. Guidelines for the rational design of Ni-based double hydroxide electrocatalysts for the oxygen evolution reaction. *ACS Catal.* **2015**, *5*, 5380−5387.
(28) Corrigan, D. A. The catalysis of the oxygen evolution reaction by iron impurities in thin-film nickel-oxide electrodes. *J. Electrochem. Soc.* **1987**, *134*, 377−384.
(29) Zhou, H. Q.; Yu, F.; Sun, J. Y.; He, R.; Chen, S.; Chu, C. W.; Ren, Z. F. Highly active catalyst derived from a 3d foam of $Fe(PO_3)_2$/Ni_2P for extremely efficient water oxidation. *Proc. Natl. Acad. Sci. U. S. A.* **2017**, *114*, 5607−5611.
(30) Biesinger, M. C.; Payne, B. P.; Grosvenor, A. P.; Lau, L. W. M.; Gerson, A. R.; Smart, R. S. C. Resolving surface chemical states in XPS analysis of first row transition metals, oxides and hydroxides: Cr, Mn, Fe, Co and Ni. *Appl. Surf. Sci.* **2011**, *257*, 2717−2730.
(31) Bediako, D. K.; Lassalle-Kaiser, B.; Surendranath, Y.; Yano, J.; Yachandra, V. K.; Nocera, D. G. Structure-activity correlations in a nickel-borate oxygen evolution catalyst. *J. Am. Chem. Soc.* **2012**, *134*, 6801−6809.
(32) Monnier, J.; Reguer, S.; Foy, E.; Testemale, D.; Mirambet, F.; Saheb, M.; Dillmann, P.; Guillot, I. XAS and XRD in situ characterisation of reduction and reoxidation processes of iron corrosion products involved in atmospheric corrosion. *Corros. Sci.* **2014**, *78*, 293−303.
(33) Wilke, M.; Farges, F.; Petit, P.-E.; Brown, G. E.; Martin, F. Oxidation state and coordination of Fe in minerals: An Fe K-XANES spectroscopic study. *Am. Mineral.* **2001**, *86*, 714−730.
(34) Westre, T. E.; Kennepohl, P.; DeWitt, J. G.; Hedman, B.; Hodgson, K. O.; Solomon, E. I. A multiplet analysis of Fe K-edge 1s → 3d pre-edge features of iron complexes. *J. Am. Chem. Soc.* **1997**, *119*, 6297−6314.
(35) Tung, C. W.; Hsu, Y. Y.; Shen, Y. P.; Zheng, Y. X.; Chan, T. S.; Sheu, H. S.; Cheng, Y. C.; Chen, H. M. Reversible adapting layer produces robust single-crystal electrocatalyst for oxygen evolution. *Nat. Commun.* **2015**, *6*, 8106.
(36) Wang, H. Y.; Hung, S. F.; Chen, H. Y.; Chan, T. S.; Chen, H. M.; Liu, B. In operando identification of geometrical-site-dependent water oxidation activity of spinel Co_3O_4. *J. Am. Chem. Soc.* **2016**, *138*, 36−39.
(37) Suen, N. T.; Hung, S. F.; Quan, Q.; Zhang, N.; Xu, Y. J.; Chen, H. M. Electrocatalysis for the oxygen evolution reaction: Recent development and future perspectives. *Chem. Soc. Rev.* **2017**, *46*, 337−365.

DOI: 10.1021/acscentsci.9b00053
ACS Cent. Sci. 2019, 5, 558−568

(38) Lassalle-Kaiser, B.; Gul, S.; Kern, J.; Yachandra, V. K.; Yano, J. In situ/operando studies of electrocatalysts using hard X-ray spectroscopy. *J. Electron Spectrosc. Relat. Phenom.* **2017**, *221*, 18−27.
(39) Busch, M. Water oxidation: From mechanisms to limitations. *Curr. Opin. Electrochem.* **2018**, *9*, 278−284.
(40) Man, I. C.; Su, H. Y.; Calle-Vallejo, F.; Hansen, H. A.; Martinez, J. I.; Inoglu, N. G.; Kitchin, J.; Jaramillo, T. F.; Norskov, J. K.; Rossmeisl, J. Universality in oxygen evolution electrocatalysis on oxide surfaces. *ChemCatChem* **2011**, *3*, 1159−1165.
(41) Rossmeisl, J.; Logadottir, A.; Norskov, J. K. Electrolysis of water on (oxidized) metal surfaces. *Chem. Phys.* **2005**, *319*, 178−184.
(42) Bediako, D. K.; Surendranath, Y.; Nocera, D. G. Mechanistic studies of the oxygen evolution reaction mediated by a nickel−borate thin film electrocatalyst. *J. Am. Chem. Soc.* **2013**, *135*, 3662−3674.
(43) Wang, L.-P.; Van Voorhis, T. Direct-coupling O_2 bond forming a pathway in cobalt oxide water oxidation catalysts. *J. Phys. Chem. Lett.* **2011**, *2*, 2200−2204.
(44) Surendranath, Y.; Kanan, M. W.; Nocera, D. G. Mechanistic studies of the oxygen evolution reaction by a cobalt-phosphate catalyst at neutral pH. *J. Am. Chem. Soc.* **2010**, *132*, 16501−16509.
(45) Bajdich, M.; Garcia-Mota, M.; Vojvodic, A.; Norskov, J. K.; Bell, A. T. Theoretical investigation of the activity of cobalt oxides for the electrochemical oxidation of water. *J. Am. Chem. Soc.* **2013**, *135*, 13521−13530.
(46) Grimaud, A.; Diaz-Morales, O.; Han, B.; Hong, W. T.; Lee, Y.-L.; Giordano, L.; Stoerzinger, K. A.; Koper, M. T. M.; Shao-Horn, Y. Activating lattice oxygen redox reactions in metal oxides to catalyse oxygen evolution. *Nat. Chem.* **2017**, *9*, 457−465.
(47) Busch, M.; Halck, N. B.; Kramm, U. I.; Siahrostami, S.; Krtil, P.; Rossmeisl, J. Beyond the top of the volcano? − a unified approach to electrocatalytic oxygen reduction and oxygen evolution. *Nano Energy* **2016**, *29*, 126−135.
(48) Halck, N. B.; Petrykin, V.; Krtil, P.; Rossmeisl, J. Beyond the volcano limitations in electrocatalysis - oxygen evolution reaction. *Phys. Chem. Chem. Phys.* **2014**, *16*, 13682−13688.
(49) Frydendal, R.; Busch, M.; Halck, N. B.; Paoli, E. A.; Krtil, P.; Chorkendorff, I.; Rossmeisl, J. Enhancing activity for the oxygen evolution reaction: The beneficial interaction of gold with manganese and cobalt oxides. *ChemCatChem* **2015**, *7*, 149−154.
(50) Darcy, J. W.; Koronkiewicz, B.; Parada, G. A.; Mayer, J. M. A continuum of proton-coupled electron transfer reactivity. *Acc. Chem. Res.* **2018**, *51*, 2391−2399.
(51) Reece, S. Y.; Hodgkiss, J. M.; Stubbe, J.; Nocera, D. G. Proton-coupled electron transfer: The mechanistic underpinning for radical transport and catalysis in biology. *Philos. Trans. R. Soc., B* **2006**, *361*, 1351−1364.
(52) Martirez, J. M. P.; Carter, E. A. Unraveling oxygen evolution on iron-doped β-nickel oxyhydroxide: The key role of highly active molecular-like sites. *J. Am. Chem. Soc.* **2019**, *141*, 693−705.
(53) Koper, M. T. M. Thermodynamic theory of multi-electron transfer reactions: Implications for electrocatalysis. *J. Electroanal. Chem.* **2011**, *660*, 254−260.
(54) Lehtimaki, M.; Hoffmannova, H.; Boytsova, O.; Bastl, Z.; Busch, M.; Halck, N. B.; Rossmeisl, J.; Krtil, P. Targeted design of alpha-MnO_2 based catalysts for oxygen reduction. *Electrochim. Acta* **2016**, *191*, 452−461.
(55) Zeng, K.; Zhang, D. K. Recent progress in alkaline water electrolysis for hydrogen production and applications. *Prog. Energy Combust. Sci.* **2010**, *36*, 307−326.
(56) Kenney, M. J.; Gong, M.; Li, Y. G.; Wu, J. Z.; Feng, J.; Lanza, M.; Dai, H. J. High-performance silicon photoanodes passivated with ultrathin nickel films for water oxidation. *Science* **2013**, *342*, 836−840.
(57) Hu, S.; Shaner, M. R.; Beardslee, J. A.; Lichterman, M.; Brunschwig, B. S.; Lewis, N. S. Amorphous TiO_2 coatings stabilize Si, GaAs, and GaP photoanodes for efficient water oxidation. *Science* **2014**, *344*, 1005−1009.
(58) Kim, T. W.; Choi, K. S. Nanoporous $BiVO_4$ photoanodes with dual-layer oxygen evolution catalysts for solar water splitting. *Science* **2014**, *343*, 990−994.
(59) Sun, K.; Saadi, F. H.; Lichterman, M. F.; Hale, W. G.; Wang, H. P.; Zhou, X. H.; Plymale, N. T.; Omelchenko, S. T.; He, J. H.; Papadantonakis, K. M.; Brunschwig, B. S.; Lewis, N. S. Stable solar-driven oxidation of water by semiconducting photoanodes protected by transparent catalytic nickel oxide films. *Proc. Natl. Acad. Sci. U. S. A.* **2015**, *112*, 3612−3617.
(60) Yeo, B. S.; Bell, A. T. In situ Raman study of nickel oxide and gold-supported nickel oxide catalysts for the electrochemical evolution of oxygen. *J. Phys. Chem. C* **2012**, *116*, 8394−8400.
(61) Fu, X.-Z.; Zhu, Y.-J.; Xu, Q.-C.; Li, J.; Pan, J.-H.; Xu, J.-Q.; Lin, J.-D.; Liao, D.-W. Nickel oxyhydroxides with various oxidation states prepared by chemical oxidation of spherical β-$Ni(OH)_2$. *Solid State Ionics* **2007**, *178*, 987−993.

DOI: 10.1021/acscentsci.9b00053
ACS Cent. Sci. 2019, 5, 558−568